

# Supporting Information for “Clustering to characterize extreme marine conditions for the benthic region of Northeastern Pacific continental margin”

Amber M. Holdsworth<sup>1</sup>, Andrew Shao<sup>2</sup>, and James R. Christian<sup>13</sup>

<sup>1</sup>Fisheries and Oceans Canada

<sup>2</sup>Hewlett Packard Enterprise

<sup>3</sup>Canadian Centre for Climate Modelling and Analysis

## Contents of this file

1. Text S1 to S4
2. Figures S1 to S13
3. Tables S1 to S3

## Introduction

The supporting information consists of additional details about model and methods used, and additional evidence for results presented in the main text. Text S1 provides additional details of regional model development and evaluation with observations (Figures S1-S5, Tables S1 and S2). Text S2 provides additional information on the cluster

---

analysis and computed thresholds (Figures S6-S8, Table S3). Text S3 provides supporting information on the compound extremes (Figures S9-S11) and event durations. Finally, Text S4 provides details of the climate indices and correlation analysis (Figures S12 and S13).

### **Text S1: North-Eastern Pacific Canadian Ocean Ecosystem Model**

This section will detail recent improvements to the model including the addition of a new module for benthic remineralization, tuning of the community structure in CanOE and evaluation of the model.

The regional ocean model, NEP36-CanOE, is an updated version of the one used in Holdsworth, Zhai, Lu, and Christian (2021), with 75 vertical levels instead of 50, a time step of 180s instead of 60s (except in the vertical), improved model bathymetry, tidal loading and attraction from Lyard, Allain, Cancet, Carrère, and Picot (2021), and the TKE scheme for vertical mixing. The biogeochemical model uses 19 tracers and each phytoplankton group has four state variables: nitrogen, carbon, iron, and chlorophyll. We have turned off iron limitation.

The model has a large computational domain with  $714 \times 1020 \times 75 = 54\,621\,000$  points. To reduce the amount of data stored on disk, we output monthly averages for the entire model and daily averages for the continental shelf (Figure S1). Only the daily averages are used for this study, and the domain is reduced to exclude open ocean regions more than 55 grid cells ( $> 100$  km) seaward of the 500 m isobath (in the x-direction). Regions where the model is not expected to perform well due to limited resolution are excluded from our analysis of extremes (Fig. S1).

We ran a perpetual cycle of the year 1996 until the model reached equilibrium (nearly repeating annual cycle). This process took 6 years for the physics and an additional 4 years with biogeochemistry turned on.

#### *Benthic remineralization parameterization*

Organic matter produced in the euphotic zone sinks through the water column. Some of it is remineralized as it sinks, and some of it is deposited on the seafloor where it is respired or buried in the sediments. Larger organisms such as clams and worms in the sediment carry out aerobic respiration, while bacteria are capable of remineralization even in the absence of oxygen (Sarmiento & Gruber, 2006). The timing, amount and freshness of the organic deposition have important consequences for the structure of benthic communities (Soetaert et al., 2000; Heip et al., 2001) and affect the timing and magnitude of sedimentary nutrient efflux and oxygen demand.

This section details the integrated sediment model that we implemented in the Canadian Ocean Ecosystem model (CanOE). The simple parameterization for the sediments that was already implemented in CanOE is known as a reflective boundary. All particulate materials deposited on the sea-floor are instantaneously transformed into nutrients and inorganic carbon in the deepest ocean layer (Soetaert et al., 2000). While the existing parameterization conserves mass and is computationally efficient, it is not particularly realistic. Bianucci, Denman, and Ianson (2011) considered these models as well as a resuspension experiment in which the organic matter reaching the seafloor remains in the lower grid cell of the water column as detritus. They found that for West Coast Vancouver Island the “resuspension” parameterization may be most appropriate because

it is a highly energetic environment (Bianucci et al., 2011). However, this region is only a small fraction of the NEP36 domain, and other regions have much less near-bottom shear and turbulence. A full diagenetic model would be computationally expensive and there is evidence that the model derived denitrification rates are significantly smaller than the true rates measured in situ (Devol, 1991). Therefore, we implemented an idealized vertically integrated model with a single sediment layer and a specified, constant fraction of remineralization as denitrification.

There are no direct measurements of sediment fluxes for the Canadian Pacific Ocean. Along the Washington State continental margin Devol (1991) and Devol and Christensen (1993) measured the benthic fluxes of  $O_2$ ,  $NH_4$ ,  $NO_3$ ,  $N_2$ ,  $Si(OH)_4$  and  $PO_4$ . These are the only direct measurements of denitrification ( $N_2$  flux) globally and relatively few shelf and slope areas have been studied (Seitzinger & Giblin, 1996).

The idealized model is conceptualized as an infinitesimally thin (essentially 2D) active layer. Organic matter deposited on the seafloor is remineralized, exchanging  $[O_2]$  and DIC with the water column. All of the organic nitrogen arriving at the seafloor is transformed to  $NH_4$  within the sediments by microorganisms in a process known as ammonification, and we assume that all of the  $NH_4$  is consumed during nitrification which demands an additional flux of  $[O_2]$  from the water column to produce  $NO_3$ . Denitrification within the sediment layer consumes all of the  $NO_3$  generated via nitrification, and the remaining demand for nitrate is supplied from the ocean model grid cell at the ocean bottom. The denitrification fraction of remineralization is fixed at 28% Devol (1991).

CanOE includes two different pools for particulate organic carbon (nitrogen): POC (PON) for the smaller class ( $1 - 100\mu\text{m}$ ) with a sinking rate  $\omega_P = 2\text{ m d}^{-1}$  and GOC (GON) for the larger class ( $100 - 5000\mu\text{m}$ ) with a sinking rate  $\omega_G = 30\text{ m d}^{-1}$  and the deposition of organic carbon to the seafloor is defined by  $\text{deposition}_C = \omega_P \text{POC}|_{z=h} + \omega_G \text{GOC}|_{z=h}$ . Organic matter in the sediment is oxidized at a rate  $r_{sedC}$  ( $\text{d}^{-1}$ ) which gives  $\text{remin}_C = F_{DIC} = r_{sedC} C_{sed}$ . Here we are assuming that remineralization (aerobic) and denitrification (anaerobic) produce the same amount of DIC (Fennel et al., 2006; Bianucci et al., 2011). The model has a single sediment pool for carbon  $C_{sed}$  from which nitrogen and iron are implicitly derived according to specified stoichiometric relationships. The change in the carbon sediment mass  $C_{sed}$  ( $\text{mmol m}^{-3}$ ) is represented by

$$\frac{dC_{sed}}{dt} = (\text{deposition}_C - \text{remin}_C). \quad (1)$$

CanOE does not assume fixed elemental ratios for phytoplankton, but it does for zooplankton and detritus; as only detritus is deposited to the sea floor, we assume Redfield stoichiometry (Redfield, 1963) for remineralization. We are assuming that remineralization is divided between aerobic and denitrification; other electron acceptors like Mn or  $\text{SO}_4^{2-}$  are assumed to be of negligible importance on the time scales considered. Although the supply of oxygen is unlikely to be limiting, this case is dealt with in the model by turning off remineralization ( $F_{DIC} = 0$ ) when there is an insufficient supply of oxygen. For simplicity, we do not allow for denitrification to occur in the absence of aerobic mineralization. We use a reflective boundary for iron, as iron is assumed to not be limiting in this environment.

We assume that the fraction of the remineralization due to denitrification is  $\gamma = 28\%$  based on Devol (1991). In the water column, CanOE assumes that a fraction of denitrification occurs via anaerobic ammonium oxidation (anammox) (Christian et al., 2022), but we do not consider anammox in the sediments. Using a balanced equation for denitrification, we define the fluxes of nitrogen and oxygen due to remineralization as

$$F_{NO_3} = -F_{DIC}(\Phi\gamma - R_{N:C}) \quad (2)$$

$$F_{O_2} = -F_{DIC}(1 - \gamma) - 2R_{N:C}F_{DIC} \quad (3)$$

where  $R_{C:O} = 1$  and  $R_{N:C} = 16/106$  are the Redfield ratios

There are also sources and sinks of alkalinity (TAlk) associated with remineralization and nitrification, a gain (1 mol TAlk / mol N) from remineralization and a loss (-2 mol TAlk / mol N) from nitrification, for a net of -1 assuming complete oxidation of all organic nitrogen to  $NO_3$  (Wolf-Gladrow et al., 2007).

$$F_{TAlk} = -R_{N:C}F_{DIC} + \gamma\Phi F_{DIC}. \quad (4)$$

For this domain, the parameterization did not make an appreciable difference in the representation of  $O_2$  or  $NO_3$  and only marginally improved the representation of DIC and TAlk.

#### *Tuning of biology parameters for the Northeastern Pacific continental margin*

The biogeochemistry model, CanOE, was originally tuned for the global ocean. The model is computationally expensive to run so a series of 6 month sensitivity tests were used to adjust the model towards the observed total chlorophyll (Department of Fisheries and Oceans Canada (DFO), 2022). We used the following criterion based on empirical

evidence in the literature: 1. Based on a wet weight of 250 (c.f. Figure 4 of Denman and Pena (2002)), peak values of mesozooplankton are expected to be around  $1.4 \text{ mmol C m}^{-3}$ , and 2. the amount of chlorophyll in diatoms should be at least 4 times greater than in nanophytoplankton for high concentrations of phytoplankton (c.f. Chisholm (1992) Figure 9).

Using 1939 ship-sampled observations of the total chlorophyll, we evaluated the model's ability to simulate productivity before (Figure S2a) and after (Fig. S2b and c) the tuning exercise. While the model and observations are only weakly correlated (Table S2), the model is now able to represent much larger values of TChl which is more appropriate for this highly productive region.

#### *Model evaluation*

The model was evaluated against available ship-sampled observations including 263 605 T and S data, 39 067  $[\text{O}_2]$ , 5 894  $[\text{NO}_3]$ , 177 [TAlk] and 237 [DIC] (Department of Fisheries and Oceans Canada (DFO), 2022). Several evaluation metrics were computed using the HydroErr toolbox (Roberts et al., 2018); the coefficient of determination (unitless), the root mean squared error signed by the bias (data units), and the Kling-Gupta decomposition (dimensionless) (Kling et al., 2012). The decomposition consists of the Pearson score  $r$  which measures the correlation, the flow variability which is a ratio of the standard deviations  $\alpha = \sigma_{\text{mod}}/\sigma_{\text{obs}}$ , the bias ratio which is a ratio of the means  $\alpha = \mu_{\text{mod}}/\mu_{\text{obs}}$  (Table S2). Values near 1 are optimal for these terms and they can be summarized using a single number known as the Kling-Gupta Efficiency (KGE). Values of  $\text{KGE} > -0.41$  mean that the model is outperforming the mean flow benchmark (Knoben et al., 2019).

The model performs better than the mean flow benchmark for all data fields and, with the exception of the total chlorophyll, all KGE efficiencies are near 1 (Table S2).

The probability density functions show that the distributions of these variables are well represented by the model (Figure S3). To evaluate how well the model represents extreme conditions, we estimated the 90<sup>th</sup> and 10<sup>th</sup> percentiles using the distributions shown in Figure S3 and (Fig. S2c). The highest concentrations of O<sub>2</sub> and TChl are not reproduced by the model. However, the focus of this study is on the lowest values, and this shows that the extremes found in the observations are well represented by the model (Table S2).

The Monthly Isopycnal / Mixed-layer Ocean Climatology (MIMOC) (Schmidtke et al., 2013) was used to evaluate the mixed layer depth (MLD) and, for consistency, the Holte and Talley (2009) algorithm was used to calculate the MLD. A series of locations along the 500 m isobath of the continental shelf were used for comparison with the monthly climatologies. We found a RMSE of 10.4 m, a KGE of 0.76, and  $R^2 = 0.92$ . The largest discrepancies occur during winter months when MLDs are deepest (Figure S4).

Tide gauge observations from 65 different stations were transformed from the Canadian Hydrographic Service (CHS) chart datum to CGDV28 (NRCan, 2022) using station specific offsets provided by CHS using their 2015 dynamic topography model. The analysis was conducted for each year, then averaged to obtain a measure for each individual station. Note that data is missing for some stations for some of the years. The average Root Mean Squared Error (RMSE) over all of the stations is  $0.33 \pm 0.17$  m ranging from 0.79 m to 0.11 m with  $R^2 = 0.95$  (Fig. S5). The performance of the tides varies spatially with



higher RMSE within the Salish Sea where the resolution may not be adequate to resolve bathymetric features.

The tidal amplitude and phase were computed for several of the tidal constituents to evaluate the model performance. The mean of the bias (model-obs) was found for each of the stations, then the average magnitude and standard deviation were computed resulting in a single value reported in Table S1. We also compute the tidal error; the RMS difference over a tidal cycle between the model and observations (Cummins and Oey (1997), eq. 3).

### *Ocean acidification*

We derive the aragonite saturation state,  $\Omega_A$  using the pyco2sys python package (Humphreys et al., 2022), and use it as a measure of the ocean acidification as it is a biologically relevant quantity. The saturation state of seawater with respect to  $\text{CaCO}_3$  is  $\Omega_A = \frac{[\text{Ca}^{2+}][\text{CO}_3^{2-}]}{K_{sp}}$  where  $K_{sp}$  is the apparent solubility product for aragonite, a distinct crystalline form of  $\text{CaCO}_3$ . When  $\Omega_A < 1$  the water is undersaturated which is conducive to shell dissolution. Model T and S are used to calculate  $K_{sp}$  and  $[\text{Ca}^{2+}]$  and  $[\text{CO}_3^{2-}]$  are calculated from modeled T, S, DIC and TAlk using pyco2sys.

### **Text S2: Clusters and thresholds**

The prevailing surface circulation west of British Columbia's continental shelf naturally divides the region into Northern and Southern regions as the Subarctic current diverges into two distinct branches; the Alaska Current flows northeast into the Gulf of Alaska and the California Current curves to the Southeast (Thomson, 1981). The bifurcation of the current occurs between  $45^\circ$  and  $50^\circ\text{N}$ , but varies seasonally so that the division is largely confined to the southeast part of the region in winter, but is highly variable in summer

when the wind patterns are more sporadic. The region west of Vancouver Island lies at the northern end of the California Current upwelling favorable zone which transitions to a downwelling favorable zone to the north. The variability in the location of the transition was part of the reason we chose to define our study regions by implementing a K-means clustering approach.

Clustering allows for a data driven estimate of regions with similar environmental conditions. By using K-means clustering using climatologies of potential temperature, AOU and aragonite saturation state (described in section 2.2 of the manuscript) instead of solely relying on expert knowledge, we reduce dependence on specialized expertise and enhance the scalability and adaptability of this methodology for broader application.

We explored using a different number of clusters and found that 6 clusters gave a reasonable set of coherent regions without an excessive amount of spatially disconnected points in the clusters. Justifying this via a traditional silhouette analysis (Murphy, 2022) (measuring the compactness of the cluster relative to the distance to the neighboring cluster) was not possible due to the strong gradients in the predictors that arise from the topography of continental slope. Essentially, increasing the number of clusters tends to pick out finer contours of the continental slope. The silhouette score thus tends to decrease monotonically as the number of points in each cluster becomes more and more varied. Visually, the Shallows and Canyons clusters do not significantly change when varying the number of clusters from 5 to 9 (not shown).

To measure the impact of the choice of the number of clusters on our analysis, we calculated the thresholds, as described in section 2.3 of the main text, for these different

cluster sizes. We found that the variance of the thresholds is  $\leq 10\%$  when using 5 to 9 clusters and  $\leq 5\%$  when using 5 to 7 clusters. The number of grid cells and climatological centres for each of the six clusters used here (Figure S6) are shown in Table S3.

For each cluster, a statistical extreme is defined using the distribution of values of dissolved oxygen, temperature and aragonite saturation state (Figure S7). The temporal division into upwelling and downwelling regimes may be unique to eastern boundary upwelling systems, but other features such as the timing of the spring freshet or melting of sea ice may be relevant if generalizing this method to other systems. The difference in the distributions for upwelling and downwelling seasons is more pronounced for the Shallows (Fig. S7).

Since all of the clusters depend on bottom depth, it's not surprising that the resulting clusters are associated with specific depth ranges (Fig. S6). Even though the clusters have some overlapping depths, they occupy unique positions in the 3D environmental space (Table S3). The two clusters selected for presentation in the paper are the Shallows (Fig. S6 d) and the Canyons (Fig. S6 a) as described in Section 2.2 and 3.1 of the main text.

Given the strong dependence of these clusters on the bottom depth, we also consider using a simpler method of grouping the benthic regions by depth. To demonstrate that clustering does a better job of identifying regions with similar environmental characteristics we found the deepest depth in the Shallows ( $\simeq 69$  m) and extracted all of the grid cells with bottom depths shallower than that depth. Comparing the locations in 3D parameter space demonstrates that the depth delineation results in a much wider range of values

(yellow diamonds in Fig. S8 (b)) for each of the three potential stressors. Many, but not all, of the points in the depth defined region are located on West Coast Vancouver Island. We plotted orange crosses to indicate the parameter space of the points (depths  $< 69$  m) north of  $51^\circ$  N which shows that temperature, AOU and  $\Omega_A$  can vary significantly at the same depth (Fig. S8 (b)). A data driven approach using machine learning to cluster the data takes the guesswork out of defining regions with similar characteristics.

Given that the goal of this paper is to study extremes, we investigated the role that temporal resolution of the data could have on the calculated thresholds. Benthic temperature was saved at 3-hour resolution. Thresholds for the Shallows and Canyons regions were calculated with 3-hour, 6-hour, 12-hour, daily, and five day averaging windows. For both the Shallows and the Canyons, during upwelling and downwelling, all resulting thresholds were within  $0.01^\circ\text{C}$  of each other. The only exception was the Shallows cluster during downwelling season where the threshold dropped by  $0.1^\circ\text{C}$  between the daily and five day averages. Therefore, we chose to limit our analysis to daily averages.

### **Text S3: Occurrence of extremes over time**

The occurrence of extremes over time is discussed in detail in section 3.2 of the manuscript. This section provides supporting information for the compound extremes, analysis of trends, and event duration for the Shallows and Canyons and provides a brief overview of our analysis for the remaining clusters.

A compound extreme is defined here as the concomitant occurrence of two or more stressors in the same grid cell. We show all of the compound extremes for the Canyons (Figure S9) and the Shallows (Figure S10) clusters, but only the triple extremes for the

remaining clusters (Figure S11). The most common compound extreme were coincident extremes in  $[O_2]$  and  $\Omega_A$ .

Some of the clusters (b, d, e, f) exhibit an increasing number of triple extremes near the end of the time series (Fig. S11), while the clusters with the deepest average depths do not (Table S3). For these deeper clusters the maximum depth of the mixed layer is typically much shallower than the ocean bottom. With less ventilation, these deeper clusters will not experience the increase in anthropogenic  $CO_2$  emissions as immediately as the shallower clusters, nor will they immediately feel the effects of near-surface marine heatwaves. However, the deeper clusters shown in Fig. S6 (c, a, and e (from deepest to shallowest)) have waters with  $\Omega_A$  at or below saturation ( $\Omega_A < 1$ ) and relatively low oxygen as a baseline (Table S3), so organisms in these regions may be particularly vulnerable to extremes in  $\Omega_A$  and  $[O_2]$ . In particular, cluster ‘e’, where groundfish biodiversity is high (Thompson et al., 2023), has baseline conditions near ecological thresholds and the deepest annual mixed layer depths are comparable with the ocean bottom depth. Triple stressor extremes are more frequent in this cluster because it is influenced by both upwelling and surface ocean extremes, especially at the end of the time series.

We analyzed the trends in single and compound extremes using linear regression and accounting for autocorrelation in the time series by calculating the effective sample size

$$N_{eff} = N \frac{1 - r_1}{1 + r_1}$$

where  $r_1$  is the lag-one autocorrelation (Bretherton et al., 1999). The only statistically significant trend ( $p > 0.05$ ) in the single stressor extremes was for  $\Omega_A$  extremes in the Shallows with the fraction of extreme waters increasing by about  $0.004 y^{-1}$ . Clusters ‘b’,

‘d’ and ‘e’ all exhibited significant trends for triple extremes, which increased at rates of  $2 \times 10^{-4} \text{ y}^{-1}$ ,  $3 \times 10^{-5} \text{ y}^{-1}$ , and  $3 \times 10^{-4} \text{ y}^{-1}$ , respectively. All three also exhibited significant trends for  $\text{O}_2/\text{T}$  extremes with similar rates, and clusters ‘b’ and ‘d’ exhibited increasing trends for  $\Omega_A/\text{T}$  extremes.

The duration of an extreme event was calculated for each grid cell, and the maximum values averaged for each cluster (Table 1 of the main text). The average duration is longer for temperature than for  $\text{O}_2$  and  $\Omega_A$  in the Canyons, while the opposite is true in the Shallows. Differences between the upwelling and downwelling seasons are generally small, but the longest duration events are in the Canyons during the downwelling season.

#### **Text S4: The influence of basin scale climate variability**

##### *Climate Indices*

Extreme conditions of hypoxia and acidification in the Canadian North Pacific are strongly influenced by changes in upwelling along the continental shelf and the ocean’s stratification and temperature. Hence, we examine the relationship between the fraction of extremes and four climate indices which are associated with variability in these conditions: the Multivariate ENSO Index (MEI), the Pacific Decadal Oscillation (PDO), The North Pacific Gyre Oscillation (NPGO) and the Bakun upwelling index (Figure S12). It is important to recognize that these indices are influenced by many processes. They are briefly described in this section.

The El Niño–Southern Oscillation (ENSO) is a recurring pattern of climate variability originating in the tropical Pacific and propagating into the extratropics by a variety of mechanisms. Different indices are used to characterize the phases of ENSO (e.g., NINO3,

NINO4, SOI). For the present study ENSO is represented using the Multivariate ENSO Index version 2 (MEI) which uses five variables from the JRA-55 reanalysis (Kobayashi et al., 2015) over the tropical Pacific basin ( $30^{\circ}\text{S} - 30^{\circ}\text{N}$  and  $100^{\circ}\text{E} - 70^{\circ}\text{W}$ ): sea level pressure, sea surface temperature, surface zonal and meridional wind, and outgoing long-wave radiation (NOAA Physical Sciences Laboratory, 2024). This index captures all of the ENSO events of the other indices and has the advantages that it does not rely on a single station or variable.

The Pacific Decadal Oscillation (PDO) is a pattern of North Pacific ( $20^{\circ}$ - $70^{\circ}\text{N}$ ) Sea Surface Temperature (SST) variability. It is the leading principal component of North Pacific SST anomalies (Mantua & Hare, 2002). The warm phase is characterized by warm ocean waters along the west coast of North America coincident with anomalously cool SSTs in the central North Pacific. The opposite pattern is observed in the cool phase. These patterns are influenced by a combination of processes (e.g., Aleutian Low) operating on different time-scales (Newman et al., 2016). The index used for this study was based on ERSSTv5, but similar results are obtained for this period using other SST datasets (Newman et al., 2016; Huang et al., 2017; NOAA Physical Sciences Laboratory, 2022).

The North Pacific Gyre Oscillation (NPGO) is defined as the second principal component of the sea surface height anomaly (SSHa) over  $180^{\circ}\text{W}-110^{\circ}\text{W}$ ;  $25^{\circ}\text{N}-62^{\circ}\text{N}$  (Di Lorenzo et al., 2008; Di Lorenzo, 2022). The SSHa and SSTa fields are highly correlated, hence, as the first and second principal components the PDO and NPGO explain the highest and second highest fraction of the variance in these fields. The NPGO is

associated with upwelling in the CCS because strengthening of the North Pacific Gyre drives more onshore flow as it flow west to east and increases Ekman transport as it flows southward in the California Current resulting in increased upwelling of low oxygen, low pH, and relatively cold water.

We used the Bakun index calculated using Sea Level Pressure on a  $3^\circ$  grid at  $48^\circ\text{N}$ ,  $125^\circ\text{W}$ , and  $51^\circ\text{N}$ ,  $131^\circ\text{W}$  (Bakun, 1973; NOAA Pacific Fisheries Environmental Laboratory, 2022). Although newer upwelling indices have been introduced, they are not appreciably different from the Bakun index at these latitudes (Jacox et al., 2018).

These indices are related to each other by the underlying processes that influence them. ENSO has been dynamically linked to the PDO (Alexander et al., 2002) through a mechanism known as an *atmospheric bridge*; ENSO excites atmospheric teleconnections in the extra-tropics influencing the variability of the Aleutian Low which, in turn, influences the PDO. Similarly, the Central Pacific Warming El Niño pattern drives atmospheric teleconnections in the central North Pacific which results in the NPGO pattern through the North Pacific Oscillation (NPO) (Di Lorenzo et al., 2023).

#### *Correlations with the climate indices*

There is reason to believe that these climate indices may have predictive power for local ecosystem changes along the continental margin of British Columbia. For example, large shifts in zooplankton taxa around Vancouver Island Mackas, Peterson, and Zamon (2004) and in the California Current system (Mackas et al., 2006) were associated with ENSO and Pacific regime shifts, Mackas et al. (2013) found that zooplankton variability in the Strait of Georgia was significantly correlated with the NPGO, Li et al. (2013) found



that the best indicator of zooplankton community change in the Strait of Georgia was the Southern Oscillation Index, Perry and Masson (2013) found that the NPGO was a leading indicator for regime shifts, Perry et al. (2021) found that the PDO was significantly related to zooplankton trends from 1996 to 2018, and Suchy, Young, Galbraith, Perry, and Costa (2022) found a significant relationship between the NPGO and the spring phytoplankton bloom.

We generated monthly averages (bi-monthly for MEI) of the time series of the fraction of extremes by combining the two different seasons. Then, we removed the seasonal cycle and normalized the datasets by subtracting the mean before calculating the cross-correlations. The cross-correlations were computed for a series of lags to better understand the temporal relationships between the variables. We computed the Pearson Correlation Coefficients (Figure S13) and, because these data may not be independent in time, we adjusted the values of  $p$  and computed the confidence intervals by considering the equivalent sample size (Von Storch & Zwiers, 2002). Assuming both signals  $X_i$  of length  $N$  are red-noise (Markov) processes the equivalent sample size is given by

$$N_{eff} = N \frac{1 - r_1 r_2}{1 + r_1 r_2}$$

where  $r_i$  is the lag-one autocorrelation for each signal (Bartlett, 1935; Bretherton et al., 1999).

The positive phase of the PDO and ENSO, and the negative phase of the NPGO, are associated with warm near-surface temperatures in the California Current System (CCS) (Di Lorenzo et al., 2008; Chhak et al., 2009) which explains why we found significant positive (negative) correlations between T extremes in the Shallows and MEI and PDO

(NPGO) (Figure S13 a, and Fig. S12 (a, b, c) ). Moreover, Amaya et al. (2023) demonstrated that ENSO influences ocean temperature extremes for the Canadian west coast via coastally trapped waves. Similar correlations were found for low oxygen extremes, indicating the strong influence of solubility on oxygen extremes for this cluster (Fig. S13 a). Extremes in  $\Omega_A$  are negatively correlated with the PDO. The warm phase of the PDO is associated with greater stratification and a deeper thermocline, resulting in less penetration of old, corrosive and oxygen-poor waters onto the continental margin.

In the Canyons,  $[O_2]$  and  $\Omega_A$  extremes both exhibit a negative correlation with the PDO and a positive correlation with the NPGO (Figure S13); both indices are associated with upwelling. The only significant correlation with the Bakun index was for temperature in the Canyons, but the correlation was weaker than those for the climate indices. The Bakun index represents the strength of upwelling/downwelling due to changes in the local winds (inferred from SLP), but other processes can contribute to upwelling in the Northern CCS (Engida et al., 2016). For example, coastally trapped waves (CTW) are excited by wind stress far to the south and propagate along the coast. They depress the thermocline, modify upwelling and influence all three stressors (Engida et al., 2016). Overall the effects of large-scale climate variability are more readily detectable in our data set than those of locally forced upwelling.

## References

- Alexander, M. A., Bladé, I., Newman, M., Lanzante, J. R., Lau, N.-C., & Scott, J. D. (2002). The atmospheric bridge: The influence of ENSO teleconnections on air–sea interaction over the global oceans. *Journal of Climate*, 15(16), 2205 - 2231. doi:

10.1175/1520-0442(2002)015<2205:TABTIO>2.0.CO;2

Amaya, D. J., Jacox, M. G., Alexander, M. A., Scott, J. D., Deser, C., Capotondi, A., & Phillips, A. S. (2023). Bottom marine heatwaves along the continental shelves of North America. *Nature Communications*, 14(1), 1038. doi: DOI={10.1038/s41467-023-36567-0}

Bakun, A. (1973). Coastal upwelling indices, west coast of North America, 1946-71 [NOAA Technical Report NMFS SSRF-671].

Bartlett, M. (1935). Some aspects of the time-correlation problem in regard to tests of significance. *Journal of the Royal Statistical Society*, 98(3), 536–543. doi: 10.2307/2342284

Bianucci, L., Denman, K. L., & Ianson, D. (2011). Low oxygen and high inorganic carbon on the vancouver island shelf. *Journal of Geophysical Research: Oceans*, 116(C7). doi: 10.1029/2010JC006720

Bretherton, C. S., Widmann, M., Dymnikov, V. P., Wallace, J. M., & Bladé, I. (1999). The effective number of spatial degrees of freedom of a time-varying field. *Journal of climate*, 12(7), 1990–2009. doi: 10.1175/1520-0442(1999)012<1990:TENOSD>2.0.CO;2

Chhak, K. C., Di Lorenzo, E., Schneider, N., & Cummins, P. F. (2009). Forcing of low-frequency ocean variability in the northeast Pacific. *Journal of Climate*, 22(5), 1255–1276. doi: 10.1175/2008JCLI2639.1

Chisholm, S. W. (1992). Phytoplankton size. In P. G. Falkowski & A. D. Woodhead (Eds.), *Primary productivity and biogeochemical cycles in the sea* (pp. 213–237).

Plenum. doi: 10.1007/978-1-4899-0762-2\_12

Christian, J. R., Denman, K. L., Hayashida, H., Holdsworth, A. M., Lee, W. G., Riche, O. G., ... Swart, N. C. (2022). Ocean biogeochemistry in the Canadian Earth system model version 5.0.3: CanESM5 and CanESM5-CanOE. *Geoscientific Model Development*, 15(11), 4393–4424. doi: 10.5194/gmd-15-4393-2022

Cummins, P. F., & Oey, L.-Y. (1997). Simulation of barotropic and baroclinic tides off northern British Columbia. *Journal of Physical Oceanography*, 27(5), 762–781. doi: 10.1175/1520-0485(1997)027<0762:SOBABT>2.0.CO;2

Denman, K., & Pena, M. (2002). The response of two coupled one-dimensional mixed layer/planktonic ecosystem models to climate change in the NE subarctic Pacific ocean. *Deep Sea Research Part II: Topical Studies in Oceanography*, 49(24-25), 5739–5757. doi: 10.1016/S0967-0645(02)00212-6

Department of Fisheries and Oceans Canada (DFO). (2022). *Institute of Ocean Sciences Data Archive* [Data set]. (Data obtained on 2022/05/15 from [www.waterproperties.ca](http://www.waterproperties.ca))

Devol, A. H. (1991). Direct measurement of nitrogen gas fluxes from continental shelf sediments. *Nature*, 349(6307), 319–321. doi: 10.1038/349319a0

Devol, A. H., & Christensen, J. P. (1993). Benthic fluxes and nitrogen cycling in sediments of the continental margin of the eastern north Pacific. *Journal of Marine Research*, 51(2), 345–372. doi: 10.1357/0022240933223765

Di Lorenzo, E. (2022). *The North Pacific Gyre Oscillation (NPGO)* [Data set]. (Data obtained on 11/25/2022 from <https://www.o3d.org/npgo/data/NPGO.txt>)

- Di Lorenzo, E., Schneider, N., Cobb, K. M., Franks, P. J. S., Chhak, K. C., Miller, A. J., ... Rivière, P. (2008). North Pacific Gyre Oscillation links ocean climate and ecosystem change. *Geophysical Research Letters*, 35(8). doi: 10.1029/2007GL032838
- Di Lorenzo, E., Xu, T., Zhao, Y., Newman, M., Capotondi, A., Stevenson, S., ... others (2023). Modes and mechanisms of Pacific decadal-scale variability. *Annual Review of Marine Science*, 15(1), 249–275. doi: 10.1146/annurev-marine-040422-084555
- Engida, Z., Monahan, A., Ianson, D., & Thomson, R. E. (2016). Remote forcing of subsurface currents and temperatures near the northern limit of the California Current system. *Journal of Geophysical Research: Oceans*, 121(10), 7244–7262. doi: 10.1002/2016JC011880
- Fennel, K., Wilkin, J., Levin, J., Moisan, J., O'Reilly, J., & Haidvogel, D. (2006). Nitrogen cycling in the Middle Atlantic Bight: Results from a three-dimensional model and implications for the North Atlantic nitrogen budget. *Global Biogeochemical Cycles*, 20(3). doi: 10.1029/2005GB002456
- Heip, C., Duineveld, G., Flach, E., Graf, G., Helder, W., Herman, P., ... others (2001). The role of the benthic biota in sedimentary metabolism and sediment-water exchange processes in the Goban Spur area (NE Atlantic). *Deep Sea Research Part II: Topical Studies in Oceanography*, 48(14), 3223–3243. doi: 10.1016/S0967-0645(01)00038-8
- Holdsworth, A. M., Zhai, L., Lu, Y., & Christian, J. R. (2021). Future changes in oceanography and biogeochemistry along the Canadian Pacific continental margin. *Frontiers in Marine Science*, 8. doi: 10.3389/fmars.2021.602991

- Holte, J., & Talley, L. (2009). A new algorithm for finding mixed layer depths with applications to Argo data and Subantarctic mode water formation. *Journal of Atmospheric and Oceanic Technology*, 26(9), 1920–1939. doi: 10.1175/2009JTECHO543.1
- Huang, B., Thorne, P. W., Banzon, V. F., Boyer, T., Chepurin, G., Lawrimore, J. H., ... others (2017). NOAA extended reconstructed sea surface temperature (ERSST), version 5. *NOAA National Centers for Environmental Information*, 30, 8179–8205.
- Humphreys, M. P., Lewis, E. R., Sharp, J. D., & Pierrot, D. (2022). Pyco2sys v1. 8: Marine carbonate system calculations in python. *Geoscientific Model Development*, 15(1), 15–43. doi: 10.5194/gmd-15-15-2022
- Jacox, M. G., Edwards, C. A., Hazen, E. L., & Bograd, S. J. (2018). Coastal upwelling revisited: Ekman, Bakun, and improved upwelling indices for the us west coast. *Journal of Geophysical Research: Oceans*, 123(10), 7332–7350. doi: 10.1029/2018JC014187
- Kling, H., Fuchs, M., & Paulin, M. (2012). Runoff conditions in the upper Danube basin under an ensemble of climate change scenarios. *Journal of Hydrology*, 424-425, 264–277. doi: 10.1016/j.jhydrol.2012.01.011
- Knoben, W. J., Freer, J. E., & Woods, R. A. (2019). Inherent benchmark or not? comparing Nash–Sutcliffe and Kling–Gupta efficiency scores. *Hydrology and Earth System Sciences*, 23(10), 4323–4331. doi: 10.5194/hess-23-4323-2019
- Kobayashi, S., Ota, Y., Harada, Y., Ebata, A., Moriya, M., Onoda, H., ... Takahashi, K. (2015). The JRA-55 Reanalysis: General specifications and basic characteristics. *Journal of the Meteorological Society of Japan. Ser. II*, 93(1), 5–48. doi: 10.2151/jmsj.2015-001

- Li, L., Mackas, D., Hunt, B., Schweigert, J., Pakhomov, E., Perry, R. I., ... Pitcher, T. J. (2013). Zooplankton communities in the Strait of Georgia, British Columbia, track large-scale climate forcing over the Pacific Ocean. *Progress in Oceanography*, 115, 90–102. doi: 10.1016/j.pocean.2013.05.025
- Lyard, F. H., Allain, D. J., Cancet, M., Carrère, L., & Picot, N. (2021). FES2014 global ocean tide atlas: design and performance. *Ocean Science*, 17(3), 615–649.
- Mackas, D., Galbraith, M., Faust, D., Masson, D., Young, K., Shaw, W., ... Sastri, A. (2013). Zooplankton time series from the Strait of Georgia: Results from year-round sampling at deep water locations, 1990–2010. *Progress in Oceanography*, 115, 129–159. doi: 10.1016/j.pocean.2013.05.019
- Mackas, D., Peterson, W., Ohman, M., & Lavaniegos, B. (2006). Zooplankton anomalies in the California Current system before and during the warm ocean conditions of 2005. *Geophysical Research Letters*, 33(22). doi: 10.1029/2006GL027930
- Mackas, D., Peterson, W., & Zamon, J. (2004). Comparisons of interannual biomass anomalies of zooplankton communities along the continental margins of British Columbia and Oregon. *Deep Sea Research Part II: Topical Studies in Oceanography*, 51(6-9), 875–896. doi: 10.1016/j.dsr2.2004.05.011
- Mantua, N. J., & Hare, S. R. (2002). The Pacific Decadal Oscillation. *Journal of oceanography*, 58(1), 35–44. doi: 10.1023/A:1015820616384
- Murphy, K. P. (2022). *Probabilistic machine learning: An introduction*. The MIT Press.
- Newman, M., Alexander, M. A., Ault, T. R., Cobb, K. M., Deser, C., Lorenzo, E. D., ... Smith, C. A. (2016). The Pacific Decadal Oscillation, revisited. *Journal of Climate*,

29(12), 4399 - 4427. doi: 10.1175/JCLI-D-15-0508.1

NOAA Pacific Fisheries Environmental Laboratory. (2022). *Traditional 3 degree Bakun index* [Data set]. National Oceanic and Atmospheric Administration. (Data obtained on 03/10/2022 from [oceanwatch.pfeg.noaa.gov/products/PFELData/upwell/monthly/upindex.mon](https://oceanwatch.pfeg.noaa.gov/products/PFELData/upwell/monthly/upindex.mon))

NOAA Physical Sciences Laboratory. (2022). *The Pacific Decadal Oscillation (PDO)* [Data set]. National Oceanic and Atmospheric Administration. (Data obtained on 12/16/2022 from <https://psl.noaa.gov/pdo/>)

NOAA Physical Sciences Laboratory. (2024). *Multivariate ENSO Index Version 2 (MEI.v2)* [Data set]. National Oceanic and Atmospheric Administration. (Data obtained on 01/11/2024 from <https://www.psl.noaa.gov/enso/mei>)

NRCan. (2022). *Geodetic reference systems* [Data set]. Natural Resources Canada. (<https://www.nrcan.gc.ca/maps-tools-and-publications/tools/geodetic-reference-systems/canadian-spatial-reference-system-csrs/9052#cgvd28>)

Perry, R. I., & Masson, D. (2013). An integrated analysis of the marine social–ecological system of the Strait of Georgia, Canada, over the past four decades, and development of a regime shift index. *Progress in Oceanography*, 115, 14–27. doi: 10.1016/j.pocean.2013.05.021

Perry, R. I., Young, K., Galbraith, M., Chandler, P., Velez-Espino, A., & Baillie, S. (2021). Zooplankton variability in the Strait of Georgia, Canada, and relationships with the marine survivals of Chinook and Coho salmon. *Plos one*, 16(1), e0245941.



doi: 10.1371/journal.pone.0245941

Redfield, A. C. (1963). The influence of organisms on the composition of seawater. *The sea*, 2, 26–77.

Roberts, W., Williams, G. P., Jackson, E., Nelson, E. J., & Ames, D. P. (2018). Hydrostats: A python package for characterizing errors between observed and predicted time series. *Hydrology*, 5(4). Retrieved from <https://www.mdpi.com/2306-5338/5/4/66> doi: 10.3390/hydrology5040066

Sarmiento, J. L., & Gruber, N. (2006). *Ocean Biogeochemical Dynamics*. Princeton: Princeton University Press. doi: 10.1515/9781400849079

Schmidtko, S., Johnson, G. C., & Lyman, J. M. (2013). MIMOC: A global monthly isopycnal upper-ocean climatology with mixed layers. *Journal of Geophysical Research: Oceans*, 118(4), 1658–1672. doi: 10.1002/jgrc.20122

Seitzinger, S. P., & Giblin, A. E. (1996). Estimating denitrification in North Atlantic continental shelf sediments. In *Nitrogen cycling in the North Atlantic ocean and its watersheds* (pp. 235–260). Springer. doi: 10.1007/BF02179829

Soetaert, K., Middelburg, J. J., Herman, P. M., & Buis, K. (2000). On the coupling of benthic and pelagic biogeochemical models. *Earth-Science Reviews*, 51(1-4), 173–201. doi: 10.1016/S0012-8252(00)00004-0

Suchy, K. D., Young, K., Galbraith, M., Perry, R. I., & Costa, M. (2022). Match/mismatch between phytoplankton and crustacean zooplankton phenology in the Strait of Georgia, Canada. *Frontiers in Marine Science*, 9, 832684. doi: 10.3389/fmars.2022.832684

Thompson, P. L., Nephin, J., Davies, S. C., Park, A. E., Lyons, D. A., Rooper, C. N., ...

Holdsworth, A. M. (2023). Groundfish biodiversity change in northeastern Pacific waters under projected warming and deoxygenation. *Philosophical Transactions of the Royal Society B: Biological Sciences*, 378(1881), 20220191. doi: 10.1098/rstb.2022.0191

Thomson, R. (1981). Oceanography of the British Columbia coast. Canadian special publication of fisheries and aquatic science. *Fisheries and Oceans Canada*, 291.

Von Storch, H., & Zwiers, F. W. (2002). *Statistical analysis in climate research*. Cambridge university press.

Wolf-Gladrow, D. A., Zeebe, R. E., Klaas, C., Körtzinger, A., & Dickson, A. G. (2007). Total alkalinity: The explicit conservative expression and its application to biogeochemical processes. *Marine Chemistry*, 106(1-2), 287–300. (Special issue: Dedicated to the memory of Professor Roland Wollast) doi: 10.1016/j.marchem.2007.01.006

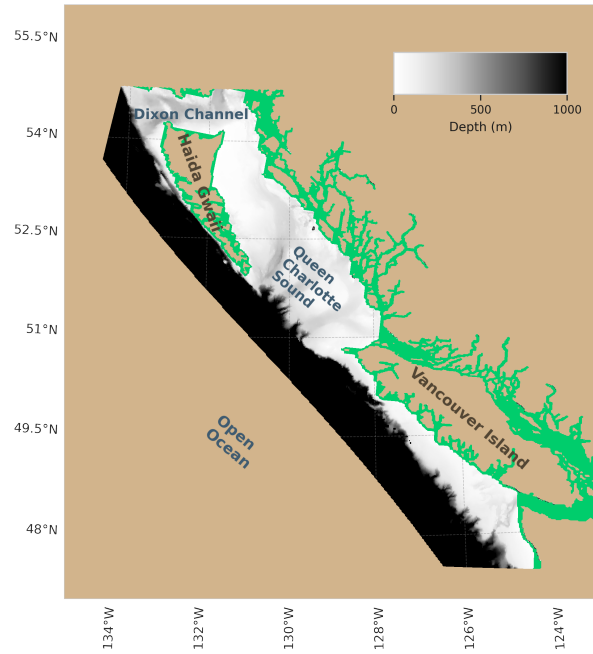


**Figure S1.** Domain and bathymetry for the analyzed model outputs. Regions excluded from analysis because the of the model's limited resolution are shown in green.

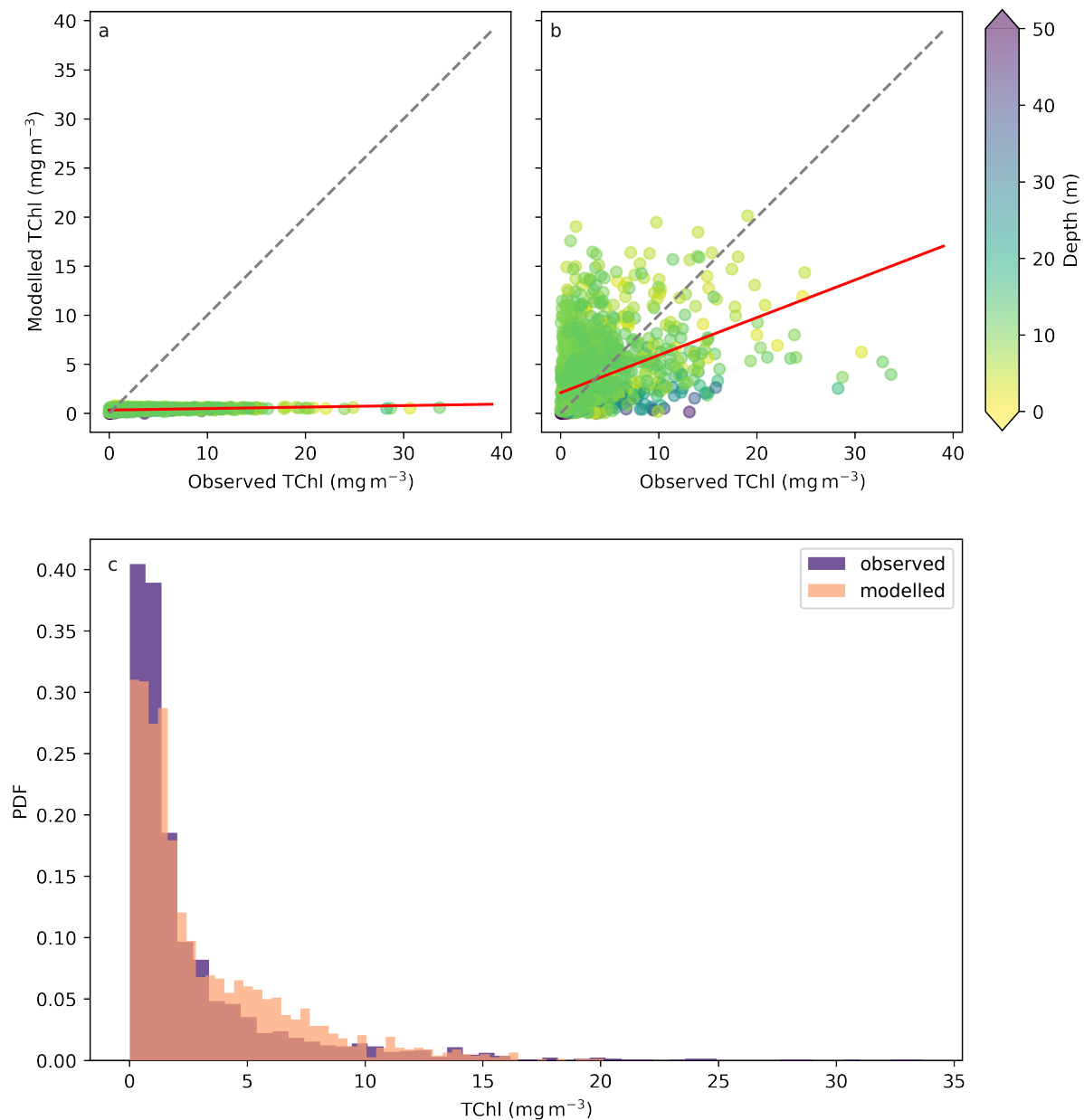


**Figure S2.** Illustration of the representation of the total chlorophyll in NEP36-CanOE with the (a) evaluation with the parameters originally developed for the global model, (b) the evaluation with the revised parameters for the Northeastern Pacific continental margin, and (c) the probability density function for the observations and revised model. The apparent third color is simply the overlapping of the other two.

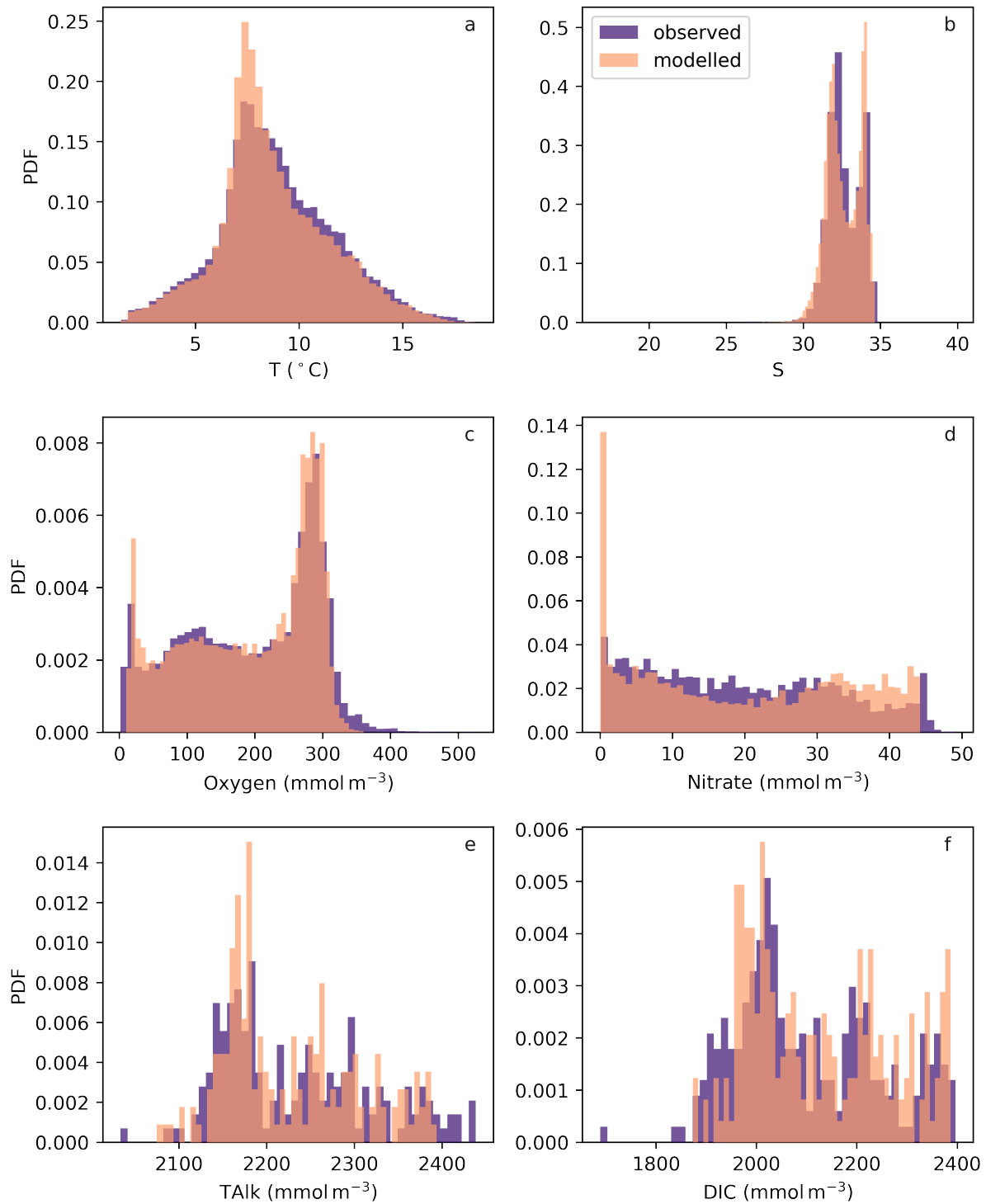


**Figure S3.** The probability density functions for the ship-sampled observations and modelled (a) potential temperature, (b) salinity, (c) oxygen, (d) nitrate, (e) total alkalinity (f) dissolved inorganic carbon. The apparent third color is simply the overlapping of the other two.

September 16, 2024, 8:39pm

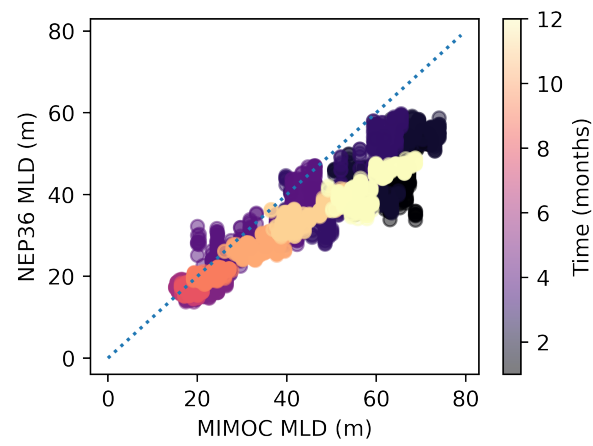


**Figure S4.** Mixed layer depths from the model plotted against the MIMOC climatology.

The colormap shows the months of the year.

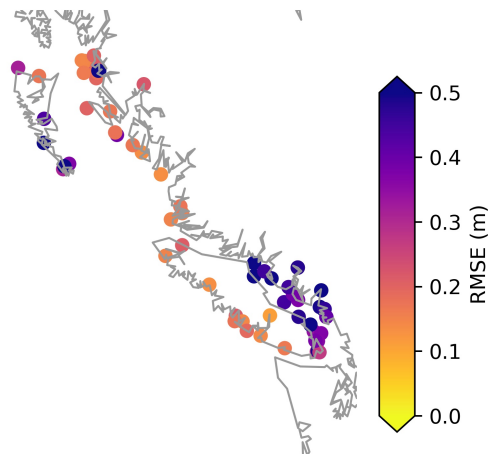


**Figure S5.** The RMSE of the total water level in the model compared with tide gauge observations.

**Table S1.** The average bias (model-observations) in the magnitude of the tidal amplitude and phase along with the tidal error associated with significant constituents.

constituent	Amplitude (m)	Phase (°)	Tide (m)
M2	$0.10 \pm 0.12$	$19.00 \pm 67.72$	$0.11 \pm 0.06$
S2	$0.03 \pm 0.03$	$6.93 \pm 8.52$	$0.04 \pm 0.02$
N2	$0.02 \pm 0.03$	$80.32 \pm 139.90$	$0.03 \pm 0.02$
K1	$0.11 \pm 0.13$	$12.05 \pm 13.79$	$0.13 \pm 0.14$
O1	$0.05 \pm 0.06$	$12.95 \pm 14.37$	$0.07 \pm 0.08$
P1	$0.04 \pm 0.05$	$12.80 \pm 14.00$	$0.04 \pm 0.05$
K2	$0.005 \pm 0.006$	$6.06 \pm 9.29$	$0.008 \pm 0.006$

**Table S2.** Evaluation of model outputs against the observations for several metrics: the signed root mean squared error (RMSE), the Pearson correlation  $r$ , the variability ratio  $\alpha$ , the bias ratio  $\beta$  and the Kling-Gupta efficiency (KGE), the bias in the 90<sup>th</sup> percentile of values and the bias in the 10<sup>th</sup> percentile of values. RMSE and biases (but not bias ratio) have the same units as their respective data fields.

variable	RMSE	r	$\alpha$	$\beta$	KGE	bias <sub>10th</sub>	bias <sub>90th</sub>
T	-0.80	0.96	0.97	0.98	0.95	.22	<b>-0.23</b>
S	-0.4	0.94	1.08	1.00	0.90	-0.18	0.004
O <sub>2</sub>	32.2	0.94	0.96	1.00	0.93	<b>-1.78</b>	-4.90
NO <sub>3</sub>	7	0.89	1.10	1.01	0.85	-1.82	2.24
DIC	51	0.95	0.96	1.01	0.93	32.6	<b>10.0</b>
TAlk	-29	0.95	0.88	1.00	0.87	<b>6.7</b>	-23.3
TChl	3.3	0.46	0.78	1.03	0.42	-0.13	1.70



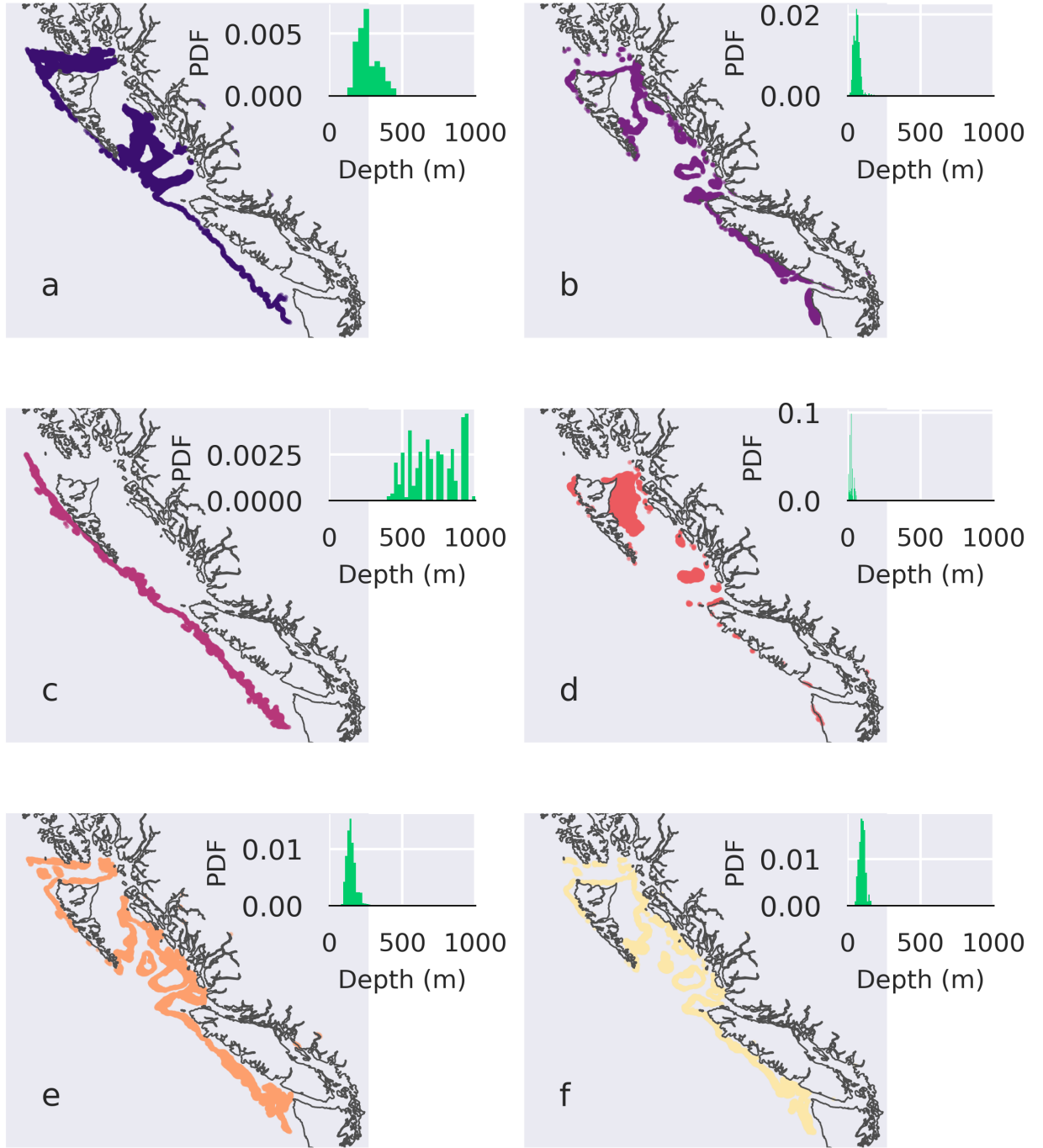


**Figure S6.** Clusters resulting from applying the K-means algorithm to climatologies of  $\Omega_A$ , AOU, and  $T$  for all bottom depths in the model less than 1000 m. The inset plot shows the distribution of benthic depths for the corresponding cluster. A more detailed description of the methodology is provided in section 2.2 of the manuscript and Text S2.

September 16, 2024, 8:39pm

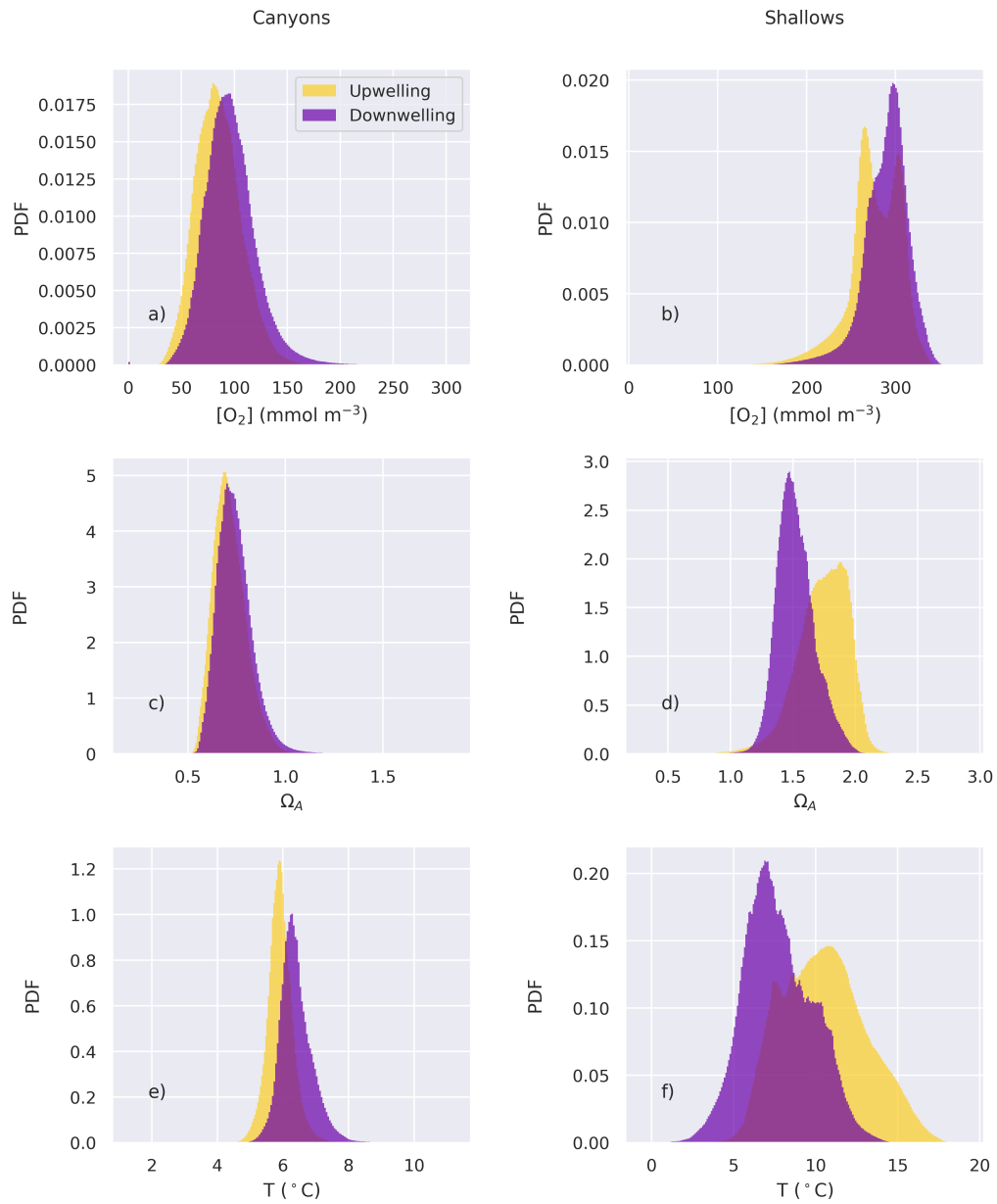


**Figure S7.** Probability density distributions for the Canyons (left) and Shallows (right) clusters (Fig. S6 a and d, respectively). Dissolved oxygen (a and d), aragonite saturation state (b and e) and temperature (c and f) are shown for each cluster with different colors for upwelling and downwelling seasons. The apparent third color is simply the overlap of the translucent distributions.

**Table S3.** For the clusters shown in Figure S6, the mean values (climatological centers), average bottom depth and average mixed layer depth (from the daily average data) are shown. The units are  $^{\circ}\text{C}$  for T,  $\text{mmol m}^{-3}$  for AOU and m for depths.

Clusters	grid cells	O <sub>2</sub>	AOU	$\Omega_A$	T	bottom depth	MLD <sub>max</sub>
a	9308	91	211	0.73	6.15	262	165
b	4005	219	71	1.3	8.3	63	74
c	3330	26	288	0.52	4.3	717	135
d	4124	282	5.3	1.63	9.1	29	36
e	7978	122	174	0.84	7.0	151	125
f	5006	168	125	1.04	7.6	101	105

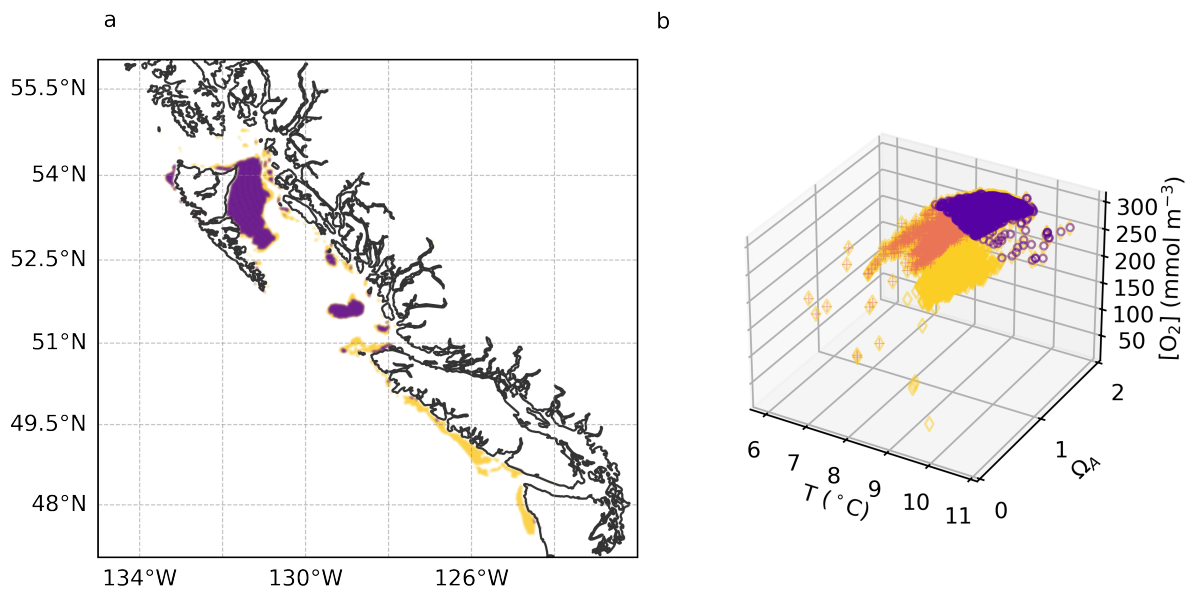


**Figure S8.** Locations of grid cells in (a) the Shallows cluster (purple) and sub-regions of grid cells with depths less than 69 m (the deepest depth in the Shallows), and (b) their relative positions in 3D parameter space.

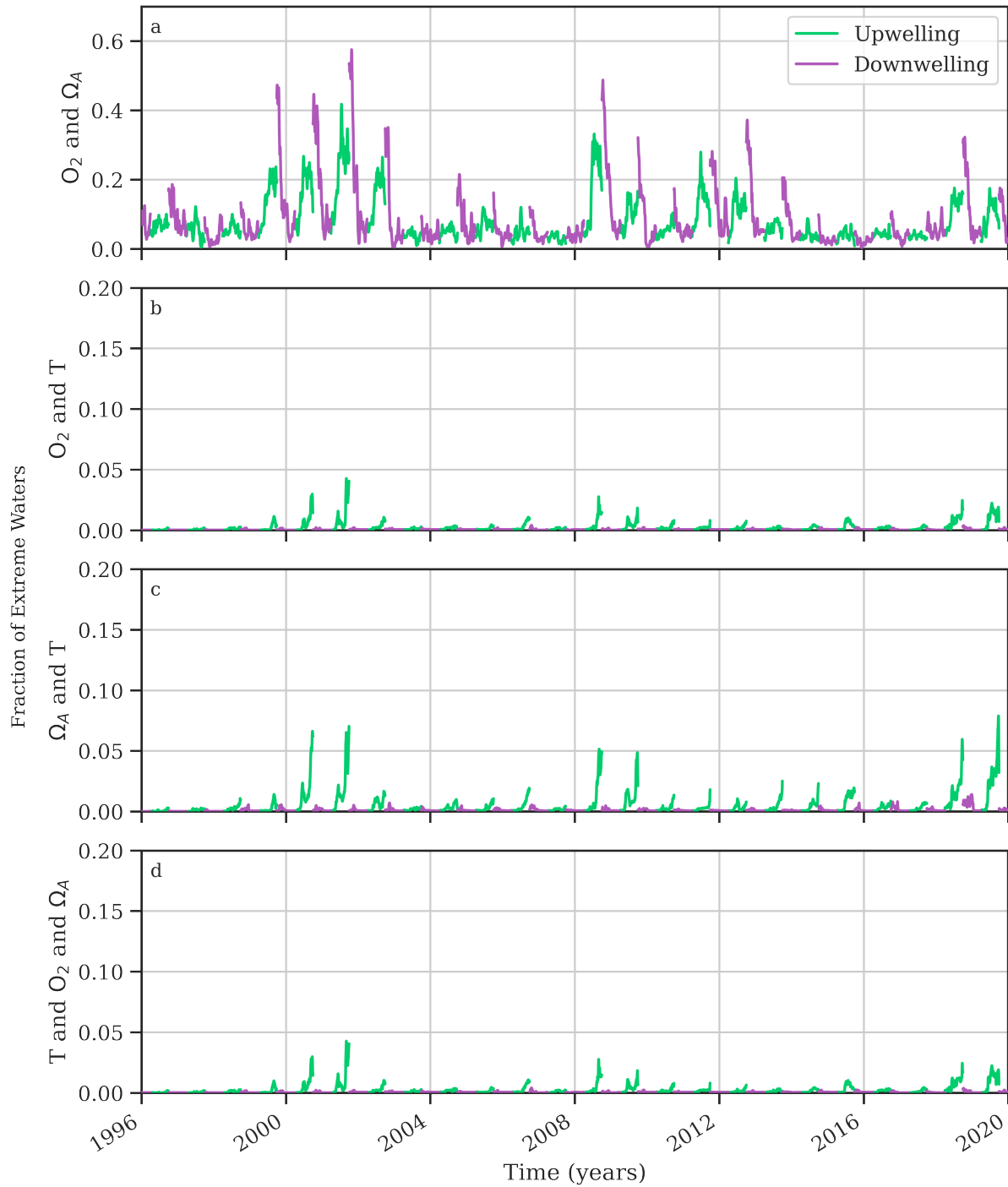


**Figure S9.** Time series of the fraction of waters in the Canyons cluster (Fig. S6 a) that experience compound extremes in (a) dissolved oxygen and aragonite saturation state, (b) dissolved oxygen and potential temperature, (c) aragonite saturation state and temperature, and (d) temperature, dissolved oxygen and aragonite saturation state.

September 16, 2024, 8:39pm

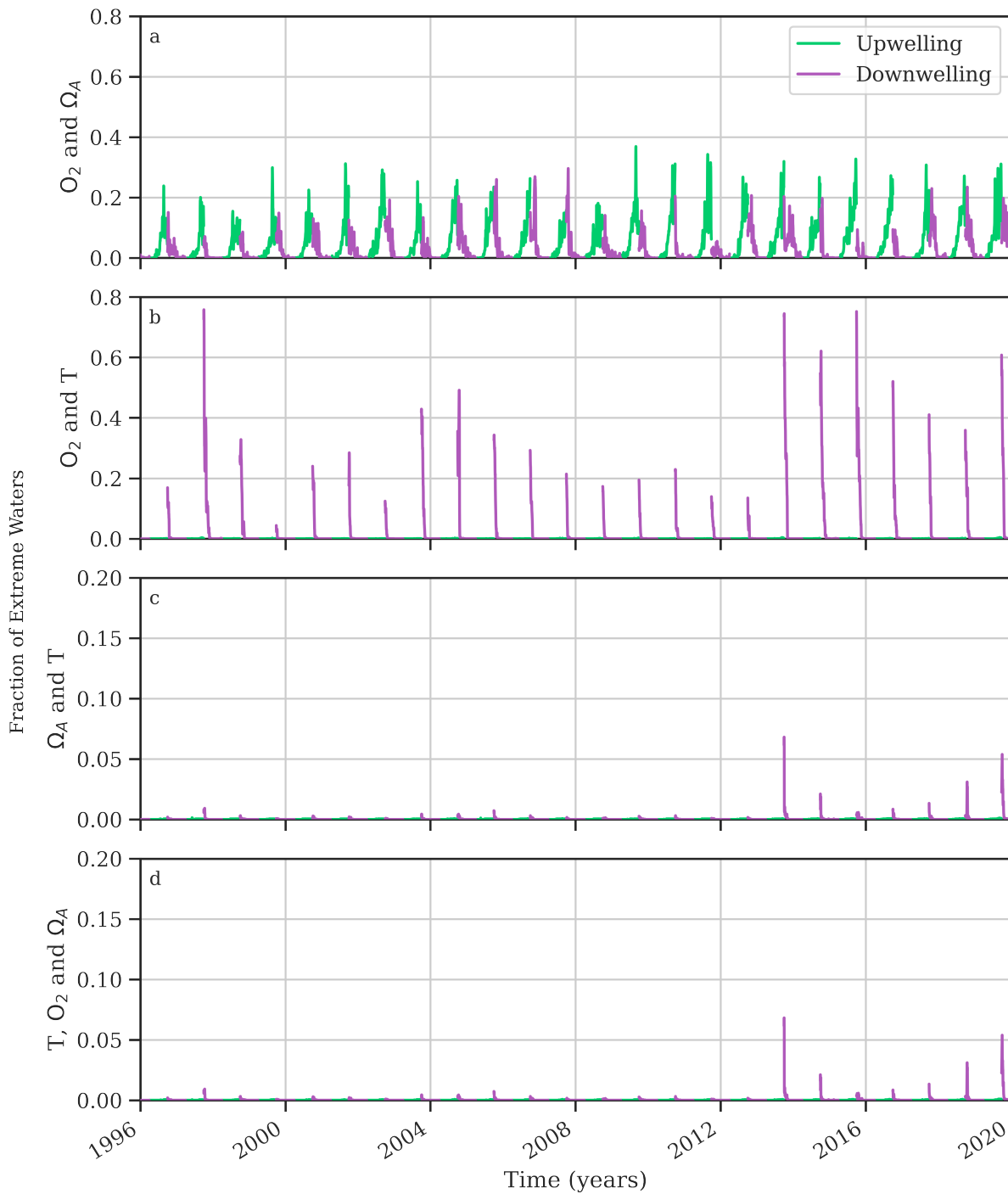


**Figure S10.** Time series of the fraction of waters in the Shallows cluster (Fig. S6 d) that experience compound extremes in (a) dissolved oxygen and aragonite saturation state, (b) dissolved oxygen and potential temperature, (c) aragonite saturation state and temperature, and (d) temperature, dissolved oxygen and aragonite saturation state.

September 16, 2024, 8:39pm

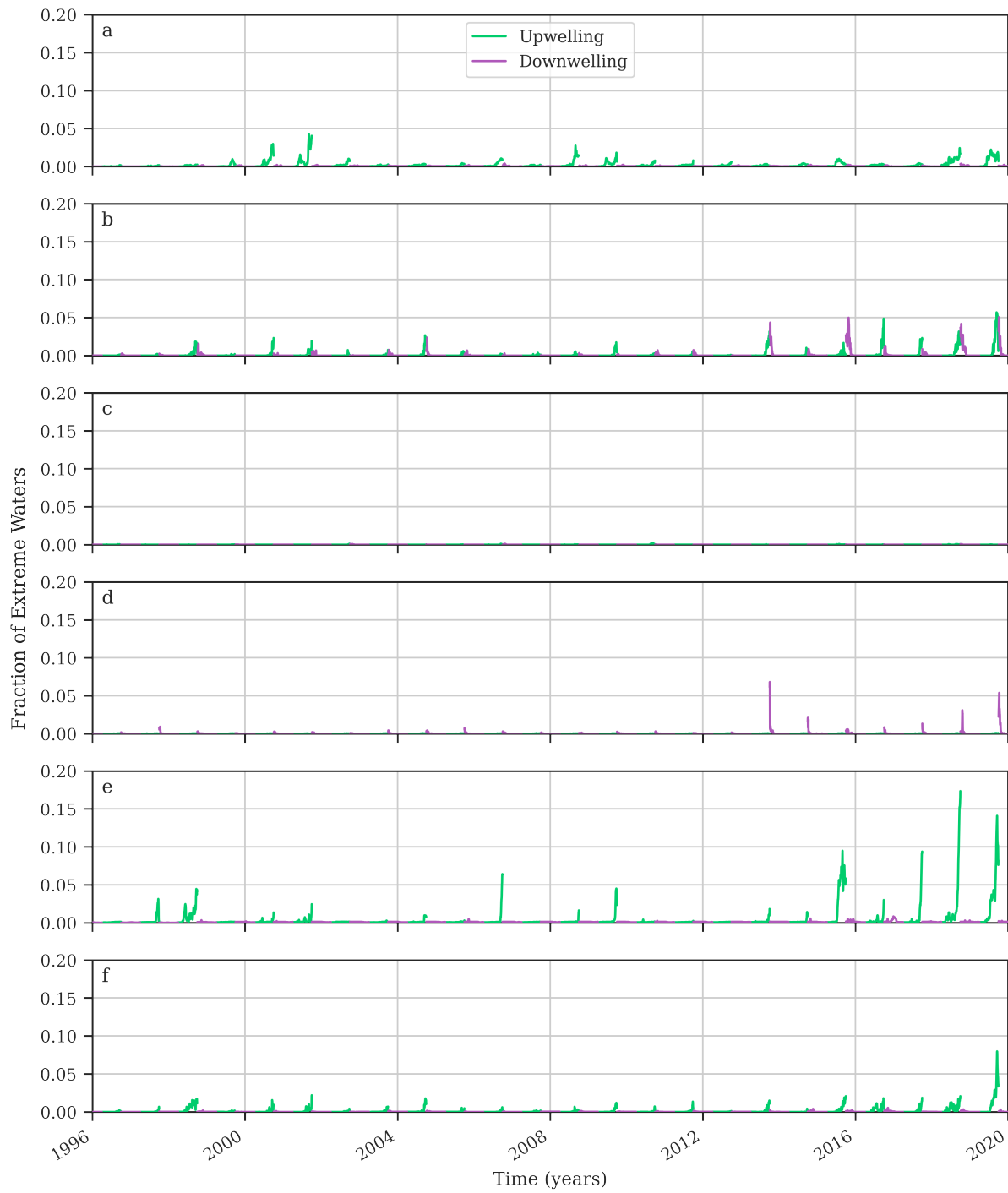


**Figure S11.** Time series of the fraction of waters that experience extremes in all three stressors (temperature, dissolved oxygen and aragonite saturation state) for all of the clusters in Fig. S6.



**Figure S12.** Time series of (a) Multivariate ENSO Index (MEI), (b) the Pacific Decadal Oscillation (PDO), (c) The North Pacific Gyre Oscillation (NPGO) and (d) the Bakun upwelling index. The indices are colored red when associated with warm water in the California Current System.



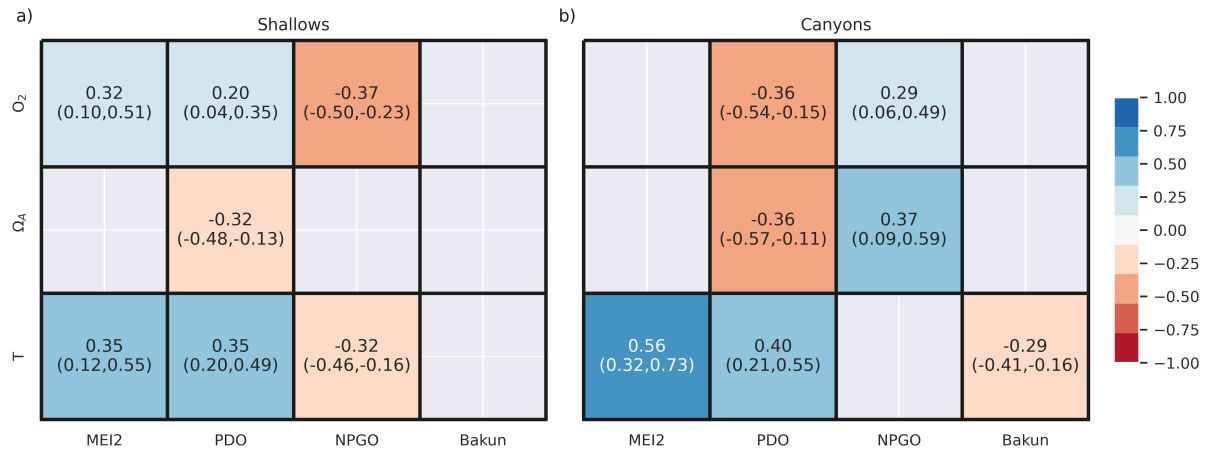


**Figure S13.** Heatmaps of the correlation between climate indices and the fraction of extreme waters in (a) Shallows and (b) Canyons clusters. The Pearson correlation coefficient is shown along with the 90% confidence interval in parentheses for cases where  $p < 0.01$  and the confidence interval does not intersect zero.